Research in Astronomy and Astrophysics, 25:055008 (13pp), 2025 May
https://doi.org/10.1088/1674-4527/adce90
CSTR: 32081.14.RAA.adce90
© 2025. National Astronomical Observatories, CAS and IOP Publishing Ltd. All rights, including for text and data mining, AI training, and similar technologies, are reserved. Printed in China.

Exploring H I Galaxy Redshift Survey Strategies for the FAST Core Array Interferometry

Zhenglong Li[1], Diyang Liu[1], Chengliang Xu[2,3], Yichao Li[1], and Xin Zhang[1,4,5]
[1] Key Laboratory of Cosmology and Astrophysics (Liaoning) & College of Sciences, Northeastern University, Shenyang 110819, China; liyichao@mail.neu.edu.cn
[2] National Astronomical Observatories, Chinese Academy of Sciences, Beijing 100101, China
[3] School of Astronomy and Space Science, University of Chinese Academy of Sciences, Beijing 100049, China
[4] National Frontiers Science Center for Industrial Intelligence and Systems Optimization, Northeastern University, Shenyang 110819, China
[5] Key Laboratory of Data Analytics and Optimization for Smart Industry (Ministry of Education), Northeastern University, Shenyang 110819, China
Received 2025 March 14; revised 2025 April 2; accepted 2025 April 9; published 2025 May 9

Abstract

We explore the feasibility of H I galaxy redshift surveys with the Five-hundred-meter Aperture Spherical Telescope (FAST) and its proposed Core Array interferometry. Using semi-analytical simulations, we compare the performance of the FAST single-dish and Core Array modes in drift scan (DS) and on-the-fly (OTF) observations across different redshifts. Our results show that the FAST single-dish mode enables significant H I detections at low redshifts ($z \lesssim 0.35$) but is limited at higher redshifts due to shot noise. The Core Array interferometry, with higher sensitivity and angular resolution, provides robust H I galaxy detections up to $z \sim 1$, maintaining a sufficient number density for power spectrum measurements and BAO constraints. At low redshifts ($z \sim 0.01$–0.08), both configurations perform well, though cosmic variance dominates uncertainties. At higher redshifts ($z > 0.35$), the Core Array outperforms the single-dish mode, while increasing the survey area has little impact on single-dish observations due to shot noise limitations. The DS mode efficiently covers large sky areas but is constrained by Earth's rotation, whereas the OTF mode allows more flexible deep-field surveys at the cost of operational overhead. Our findings highlight the importance of optimizing survey strategies to maximize FAST's potential for H I cosmology. The Core Array is particularly well-suited for high-redshift H I galaxy surveys, enabling precise constraints on large-scale structure and dark energy.

Key words: (cosmology:) large-scale structure of universe – cosmology: observations – methods: observational – surveys

1. Introduction

Hydrogen is the most abundant element in the universe. After the epoch of reionization (EoR), the neutral hydrogen (H I) is widely distributed within galaxies and plays a crucial role as a tracer for large-scale structure (LSS) surveys of the universe via its 21 cm emission line of hyperfine spin-flip transition (e.g., Battye et al. 2004; McQuinn et al. 2006; Pritchard & Loeb 2012).

However, resolving the H I emission line individually from the distant galaxies at centimeter wavelength needs large radio interferometers and it is also time-consuming. Limited by the current radio telescope resolution and sensitivity, the H I galaxy surveys can only be carried out within a small cosmic volume (e.g., Barnes et al. 2001; Meyer et al. 2004; Zwaan et al. 2004; Lang et al. 2003; Giovanelli et al. 2005, 2007; Saintonge 2007). Instead, by measuring the total H I intensity of several galaxies within large voxels, known as the H I IM (Chang et al. 2008; Loeb & Wyithe 2008; Mao et al. 2008; Pritchard & Loeb 2008; Wyithe & Loeb 2008; Wyithe et al. 2008; Peterson et al. 2009; Bagla et al. 2010; Seo et al. 2010; Lidz et al. 2011; Ansari et al. 2012; Battye et al. 2013), can quickly be carried out and extended to a large cosmic survey volume, making it particularly suitable for cosmological surveys. (Xu et al. 2015; Jin et al. 2021; Zhang et al. 2021; Wu & Zhang 2022; Wu et al. 2023a, 2023b; Zhang et al. 2023; Pan et al. 2025).

The H I IM technique has been investigated by analyzing the cross-correlation function between a Green Bank Telescope (GBT) H I IM survey and an optical galaxy survey (Chang et al. 2010). Subsequent studies reported several detections of the cross-correlation power spectrum using H I IM data from GBT and Parkes telescopes cross-correlated with optical galaxy surveys (Masui et al. 2013; Anderson et al. 2018; Wolz et al. 2017, 2022; Amiri et al. 2023). Various ongoing H I IM experiments target the post-reionization epoch. Examples include the Tianlai project (Chen 2012; Li et al. 2020; Wu et al. 2021; Perdereau et al. 2022; Sun et al. 2022) and the Canadian Hydrogen Intensity Mapping Experiment (CHIME; Bandura et al. 2014). Upcoming H I IM experiments under development include the Baryonic Acoustic Oscillations from Integrated Neutral Gas Observations (BINGO; Battye et al. 2013) and the Hydrogen Intensity and Real-Time Analysis

Experiment (HIRAX; Newburgh et al. 2016). The H I IM technique is also a central focus for cosmological studies with the Square Kilometre Array (SKA; Santos et al. 2015; Square Kilometre Array Cosmology Science Working Group et al. 2020; Zhang et al. 2019) and MeerKAT (Bull et al. 2015; Santos et al. 2017; Li et al. 2021; Paul et al. 2021; Wang et al. 2021; Chen et al. 2023). Recently, a cross-correlation power spectrum detection between MeerKAT H I IM data and an optical galaxy survey has been reported (Cunnington et al. 2023; MeerKLASS Collaboration et al. 2025; Carucci et al. 2024). However, the H I auto-power spectrum is still under detection with H I IM (Switzer et al. 2013; Paul et al. 2023).

However, a significant challenge for the H I IM survey is effectively removing foreground contamination (Wolz et al. 2015; Spinelli et al. 2022). This issue is further complicated by various systematic effects, such as the primary beam leakage (Matshawule et al. 2021), polarization calibration errors (Liao et al. 2016), correlated noise (Harper et al. 2018; Hu et al. 2021; Li et al. 2021), etc. Efforts are currently underway to address and mitigate these systematic challenges (Ni et al. 2022; Gao et al. 2023; Irfan et al. 2024). Alternatively, the H I galaxy surveys, which are free of foreground contamination, could be carried out with an efficiently large cosmic volume by utilizing next-generation radio interferometer arrays. Prominent examples include the SKA, the next-generation Very Large Array (ngVLA; Murphy et al. 2018), and the synthesis-array-upgraded Five-hundred-meter Aperture Spherical Telescope (FAST), referred to as the FAST Core Array (Jiang et al. 2024).

FAST is the largest single-dish telescope in the world (Nan & Li 2013), and since it was completed and operational in 2020 February, it has succeeded in making a number of new discoveries and interesting observations. As the most sensitive telescope, FAST shows considerable potential for cosmological studies via the H I IM technique (Li & Ma 2017; Hu et al. 2020) and is proposed with different drift scan cosmological surveys, e.g., the FAst neuTral HydrOgen intensity Mapping ExpeRiment (FATHOMER; Li et al. 2023; Zhao et al. 2024; Liu et al. 2024) and H I cosmology projects with the Commensal Radio Astronomy FasT Survey (CRAFTS; Li et al. 2018; Yang et al. 2024). Currently, the H I galaxy surveys with FAST are still limited within the lower redshift (Hu et al. 2020; Zhang et al. 2024).

The FAST Core Array, proposed by the FAST Operation and Development Center, aims to ensure that China remains competitive in the field of next-generation radio astronomy facilities through the 2030s. Another key goal is to serve as a proof-of-concept for the future FAST Array (FASTA; Xue et al. 2023), offering crucial technical insights and identifying potential challenges that may arise during the implementation of FASTA. With substantial improvements in sensitivity and angular resolution, the FAST Core Array offers significant potential as an ideal instrument for future H I galaxy cosmological redshift surveys. This study employs semi-analytical simulation data to provide a detailed analysis of observation strategies for the FAST Core Array, aimed at optimizing its performance in upcoming H I galaxy cosmological redshift surveys.

The rest of this paper is organized as follows. In Section 2, we describe the semi-analytical simulation data used in this study. Section 3 outlines the potential observation strategies that could be implemented with the FAST Core Array. In Section 4, we evaluate the effects of these strategies on H I galaxy surveys and present forecasts for the measurement uncertainties of the H I galaxy power spectrum. Finally, our conclusions are summarized in Section 5.

2. Simulation Data

We utilize a semi-analytical simulation to estimate the galaxy number density observable with future FAST Core Array H I galaxy surveys. This simulation is based on the JiuTian-1G (JT1G) simulation (Pei et al. 2024), a large-scale dark matter-only *N*-body simulation developed within the framework of Λ cold dark matter (ΛCDM) cosmology, designed for next-generation surveys. The JT1G simulation was conducted using the L-GADGET-3 code (Springel et al. 2001; Springel 2005; Angulo et al. 2012), within a cubic volume of $1\,h^{-1}$Gpc on each side. It achieves a particle mass resolution of $3.72 \times 10^8\,h^{-1}M_{\odot}$ and includes 128 snapshots spanning redshifts from 128 to 0.

The galaxy catalog is constructed using the advanced semi-analytical model L-GALAXY (Henriques et al. 2017), modified to enhance the treatment of satellite galaxy disruption (Pei et al. 2024). For each galaxy, the L-GALAXY model provides the total cold hydrogen gas mass. Following the cosmic evolution framework for the atomic and molecular phases of cold hydrogen gas, the H I and molecular hydrogen (H_2) masses are assigned based on the total cold gas mass and additional galaxy properties (Obreschkow et al. 2009). The H I profile is constructed via the analytical H I and circular velocity profile models developed by Obreschkow et al. (2009). We adopt the observational frame H I line widths, $\Delta V_{\rm o}$, measured at the 50 percentile level of the peak flux densities. Finally, the snapshots are assembled into a light cone covering a redshift range from 0 to 1, spanning a sky area of $20^{\circ} \times 20^{\circ}$.

The total H I flux integrated over the galaxy velocity profile is estimated via (Meyer et al. 2017),

$$\frac{S_{\rm HI}}{\rm Jy\ km\ s^{-1}} = \frac{(1+z)^2}{2.35 \times 10^5} \frac{M_{\rm HI}}{h^{-2}{\rm M}_{\odot}} \left(\frac{d_{\rm L}(z)}{h^{-1}{\rm Mpc}} \right)^{-2}, \quad (1)$$

where $M_{\rm H\,I}$ is the H I mass and $d_{\rm L}(z)$ is the luminosity distance to the galaxy at redshift of z.

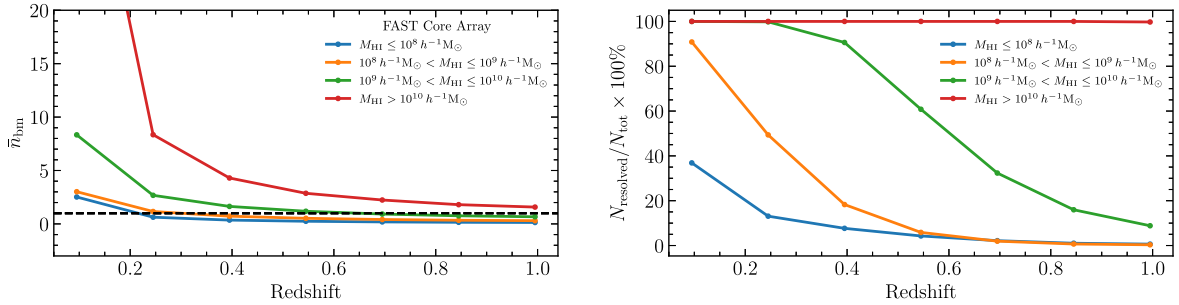

Figure 1. The galaxies resolved by the FAST Core Array as the function of redshift. Left panel: the mean number of beams covered by galaxies as the function of redshift. The dashed horizontal line indicates $\bar{n}_{\rm bm} = 1$. Right panel: the fraction of the galaxies can be resolved by the FAST Core Array as the function of redshift. In both panels, the galaxies are grouped into different H I mass bins, and the corresponding results are shown in different colors, respectively.

3. Observation Strategies for H I Galaxy Survey

The H I galaxy detection signal-to-noise ratio (SNR) is estimated via (Saintonge 2007),

$$\mathrm{SNR} = \frac{S_{\rm HI}/\Delta V_{\rm o}}{\sigma_{\rm bm}} \times \left(\frac{n_{\rm ch}}{n_{\rm bm}}\right)^{1/2}, \quad (2)$$

where $S_{\rm H\,I}/\Delta V_{\rm o}$ represents the mean H I flux density of the galaxy, $n_{\rm ch}$ is the number of velocity channels the H I profile spans, $\sigma_{\rm bm}$ is the flux density rms raised by the noise within the beam area. Due to the large aperture of the FAST telescope, nearby galaxies may be spatially resolved. Additionally, with the FAST Core Array, a significant number of galaxies, particularly massive ones, can be resolved. So an extra factor $\left(\frac{1}{n_{\rm bm}}\right)^{1/2}$ is applied to show the effect of galaxy resolution on detection, where $n_{\rm bm}$ is the number of beams covered by resolved galaxies, and is equal to one for unresolved galaxies.

The fraction of resolved galaxies may vary across different redshifts. Assuming a beam size of the FAST Core Array, we estimate the mean number of beams covered by the galaxies denoted as $\bar{n}_{\rm bm}$, within different redshift bins using the simulated catalog. The results are presented in the left panel of Figure 1. Additionally, we categorize galaxies based on their H I mass, with the corresponding results shown in different colors. Our findings indicate that galaxies with a H I mass greater than $10^{10}\,h^{-1}{\rm M}_\odot$ can be well resolved up to a redshift of $z \sim 1$. Furthermore, we estimate the fraction of galaxies that can be resolved by the FAST Core Array, as shown in the right panel of Figure 1. The results demonstrate that, except for the most massive galaxies with H I masses exceeding $10^{10}\,h^{-1}M_\odot$, the fraction of resolved galaxies decreases with increasing redshift.

The single-dish observations can be carried out with either a single FAST telescope or 24 individual 40 m dishes. The $\sigma_{\rm bm}$ is estimated with,

$$\sigma_{\rm bm}^{\rm single} = \sqrt{2}\frac{k_{\rm B}T_{\rm sys}}{A_{\rm eff}}\frac{1}{\sqrt{N_{\rm dish}\,\Delta t\Delta\nu}}, \quad (3)$$

where $k_{\rm B}$ is the Boltzmann constant, $T_{\rm sys}$ is the system temperature, $A_{\rm eff}$ is the effective aperture area, $\Delta\nu$ is the frequency resolution, Δt is the total integration time within the beam area. For FAST single dish observation, $N_{\rm dish} = 1$, and for the single dish observation with 40 m dishes, $N_{\rm dish} = 24$.

The system temperature is $T_{\rm sys} = T_{\rm rec} + T_{\rm sky}$, where $T_{\rm rec}$ is the receiver temperature. With sky area away from the Galactic plane, $T_{\rm sky}$ is modeled as (Hu et al. 2020)

$$T_{\rm sky} = 2.73 + 25.2 \times (0.408/\nu_{\rm GHz})^{2.75} K. \quad (4)$$

With the future FAST Core Array, the H I galaxy surveys can also be carried out with interferometers, which consist of either a sub-array with only the 24 40 m dishes, or the entire array including the FAST telescope. The flux density variance raised by noise within the synthesis beam area is estimated via,

$$\sigma_{\rm bm}^{\rm array} = \sqrt{2}\frac{k_{\rm B}T_{\rm sys}}{A_{\rm eff}}\frac{1}{\sqrt{N_{\rm dish}(N_{\rm dish}-1)\,\Delta t\Delta\nu}}. \quad (5)$$

For the interferometry array consisting of only the 24 40 m dishes, $A_{\rm eff}$ is the effective aperture area of the 40 m dish. However, for the interferometry array including the FAST dish, we adopted the mean effective aperture (Xu et al. 2025),

$$\overline{A_{\rm eff}} = \sqrt{N'_{\rm dish}A_{\rm eff}^{\rm FAST}A_{\rm eff}^{\rm 40m} + \frac{N'_{\rm dish}(N'_{\rm dish}-1)}{2}(A_{\rm eff}^{\rm 40m})^2}, \quad (6)$$

where $N'_{\rm dish} = N_{\rm dish} - 1 = 24$ is the number of dishes in the 40 m array, $A_{\rm eff}^{\rm FAST}$ and $A_{\rm eff}^{\rm 40m}$ represent the effective aperture area of the FAST and 40 m dish, respectively. Assuming equivalent aperture efficiency at 0.7, the effective collecting area is estimated to be approximately 50,000 $\rm m^2$ for FAST and 880 $\rm m^2$ for a 40 m dish. Substitution of these values into Equation (6) yields a mean effective aperture of about 35,470 $\rm m^2$ for the full FAST Core Array.

The integration time within the beam area, δt, is estimated according to different observation strategies. In this work, we consider two different observation modes, i.e., the drift scan (DS) and on-the-fly (OTF) observation modes, for both the

FAST single dish and the FAST Core Array interferometer observation.

3.1. Drift Scan Survey

Considering a total DS survey area of $S_{\rm area}$, the total integration time within the beam area is estimated via,

$$\Delta t = \delta t \times \left(N_{\rm tot}/\frac{S_{\rm area}}{\delta S}\right), \quad (7)$$

where δt and δS are the integration time and the survey area with one stripe of a DS observation. $S_{\rm area}/\delta S$ represents the number of stripes required to cover the survey area, and $N_{\rm tot} = t_{\rm tot}/t_0$ is the total number of stripes within a total observation time $t_{\rm tot}$, where t_0 is the observation time spent on one DS stripe. In this work, we assume that every night, we could only finish one stripe observation with $t_0 = 4$ h, which spans an R.A. range of 60 deg.

The sky drifts across with a speed of $\omega_{\rm e}\cos\delta$ in a DS survey, where $\omega_{\rm e} \approx 0.^{\prime}25\ {\rm s}^{-1}$ is the angular velocity of the rotation of the Earth, and δ is the decl. of the pointing direction. The integration time for drifting across a pixel of the beam size is given by

$$t_{\rm bm}(z) = \frac{\theta_{\rm FWHM}(z)}{\omega_{\rm e}\cos\delta}, \quad (8)$$

where $\theta_{\rm FWHM}(z)$ represents the beam size at redshift z defined as the full width at half maximum (FWHM) of the beam profile. Considering the survey targeting at the sky close to the zenith of the FAST site, i.e., $\delta \sim 26°$, the integration time per beam can be estimated as:

$$\frac{t_{\rm bm(z)}}{s} = 4.46\frac{\theta_{\rm FWHM}(z)}{\rm arcmin}, \quad (9)$$

The beam size increases with increasing redshift, resulting in a larger area covered by the scan strip and integration time per beam. To simplify computations, the subsequent analysis assumes a constant beam size across the designated frequency band, providing a conservative prediction.

During DS observation, rotating the FAST 19-feed array to $23.^{\circ}4$ ensures that the spacing between the inner beams achieves super-Nyquist sampling, meaning it is smaller than half of FWHM (Li et al. 2018). This beam overlap effectively increases the integration time per sky position compared to a single-beam observation, enhancing sensitivity and improving survey efficiency. Using the actual beam positions and beam widths from (Jiang et al. 2020), we simulate the integration time enhancement due to beam overlapping, $t_{\rm OL}$, at redshifts $z = 0.05$ and $z = 0.35$. The results for different pointing declinations are shown in Figure 2.

The initial per-beam integration time, $t_{\rm bm}$, varies smoothly with the pointing angle, following an inverse proportionality to the scan speed, which scales with the cosine of the decl., peaking at the celestial equator. The beam-overlapping-enhanced integration time, $t_{\rm OL}$, exhibits a similar trend but becomes less reliable at larger pointing angles. This limitation arises because the reduced scan speed at large angles, coupled with the finite simulation resolution, prevents accurate modeling of beam overlap. Nevertheless, the ratio of the 19-beam to single-beam integration time can be estimated as approximately 1.6 at $z = 0.05$ and 2.6 at $z = 0.35$, demonstrating the significant integration time enhancement enabled by beam overlapping in the DS mode.

FAST L-band 19 Feeds. For the DS survey with FAST *L*-band 19 feeds, we adopt the beam size $\theta_{\rm FWHM}(z) = 2.9(1 + z)$ arcmin. The effective frequency range of the FAST *L*-band for H I survey spans from 1.05 GHz to 1.40 GHz, corresponding to redshift up to $z \sim 0.35$. The integration time per beam spans from $t_{\rm bm}(z = 0.05) \simeq 13.7$ s to $t_{\rm bm}(z = 0.35) \simeq 17.4$ s. The field of view (FoV) of the feed array can be estimated as a circular area with a diameter of ∼22 arcmin, since the largest angular distance of the beam center to that of the central beam is ∼11.6 arcmin (Jiang et al. 2020). Therefore, with a 4 hr DS observation, the 19 feeds cover a sky stripe with an area of $\delta S \simeq 22$ arcmin × 60 deg $\simeq 22$ deg^2. Considering the enhancement due to the beam overlapping, the integration time increased by 1.6 times at $z = 0.05$ and thus achieved an integration time of $\delta t \simeq 1.6 \times t_{\rm bm}(0.05) \simeq 22$ s per beam.

FAST UHF-band PAF. Considering the DS survey runs at the ultra-high frequency (UHF) band with the upgraded phased array feed (PAF), we assume that the square-positioned PAF forms 10 × 10 beams covering an FoV of 36 × 36 arcmin^2 and works in the frequency range of 0.55–1.05 GHz (Han & Zhong 2016; Hu et al. 2020), corresponding to the redshift range of 0.35–1.58. With a 4 hr DS observation, the PAF covers a sky stripe with an area of $\delta S \simeq 36$ arcmin × 60 deg $\simeq 36$ deg^2 and the integration time per beam area is $\delta t = 10 \times t_{\rm bm}(0.35) \simeq 174$ s, where the factor 10 represents the repeating observations of the 10 beams, if they are aligned with the scanning direction.

FAST Core Array L-band. For the DS survey carried out with the future FAST Core Array, the FoV of the interferometer observation is restricted by the minimal one of the FAST dish and the 40 m dish. However, the FoV of FAST is restricted by the arrangement of 19 feeds and the beam size variation across frequencies is negligible. Therefore, it can simply be estimated as ∼0.1 deg^2 using the diameter aforementioned, while that of the 40 m dish can be estimated with a diameter at ∼18′ at 1.4 GHz (Jiang et al. 2024). As shown in Figure 3, the FoV of the 40 m dish (solid blue) is smaller than that of FAST (dashed red) up to $z = 0.22$, indicating that the 40 m dish provides a more conservative estimate for the high-frequency sub-band, while FAST becomes the better choice for the low-frequency sub-band. Despite these differences, the survey is conducted in the *L*-band as a whole. More importantly, the high-frequency sub-band experiences less contamination from radio frequency interference (RFI), requiring fewer flagged data points (see (Li et al. 2023) for details). Consequently, we adopt the FoV of the 40 m dish at $z = 0.05$, corresponding to an FoV diameter of

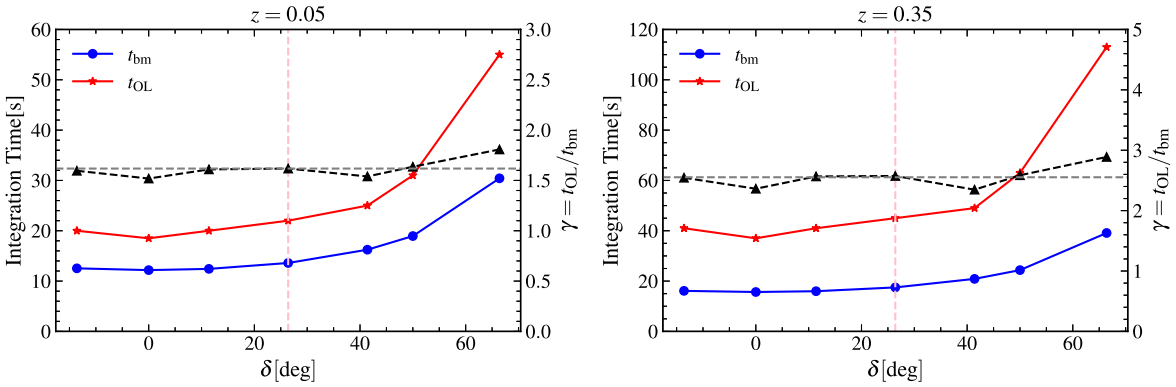

Figure 2. The integration time enhancement due to beam overlapping in DS observation at different pointing declinations. The left and right panels correspond to redshifts $z = 0.05$ and $z = 0.35$, respectively. The beam-overlapping-enhanced integration time, $t_{\rm OL}$, and the initial per-beam integration time, $t_{\rm bm}$, are shown in red and blue on the left axis, while their ratio, $\gamma = t_{\rm OL}/t_{\rm bm}$, is displayed in black on the right axis. The pink dashed line marks the decl. corresponding to the zenith angle of the FAST site, and the gray dashed line represents the mean ratio across different pointing angles.

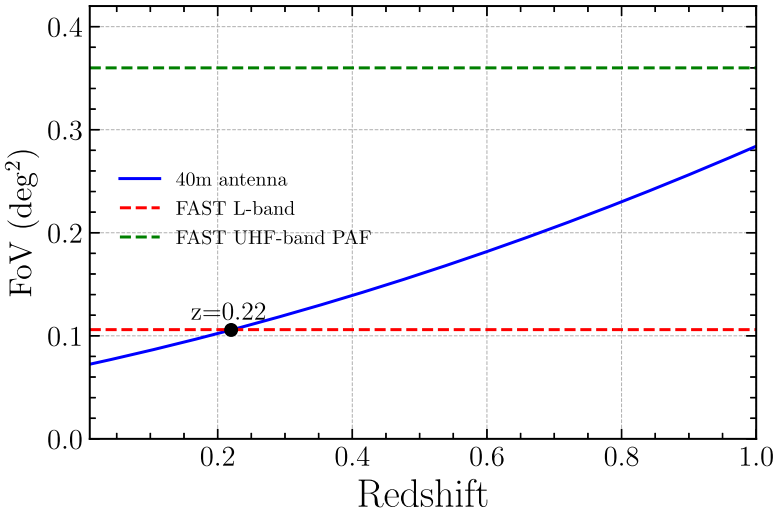

Figure 3. Comparison of the FoV of 40 m antenna (blue solid), FAST *L*-band 19 feeds (red dashed), and FAST UHF-band PAF (green dashed).

19′, as the reference FoV for *L*-band observations with the FAST Core Array interferometer. With a 4 hr DS observation, the interferometer observation at the *L*-band covers a sky stripe with an area of $\delta S \simeq 19$ arcmin $\times$ 60 deg $\simeq 19$ deg^2 and the integration time per beam area is $\delta t \simeq t_{\rm bm}^{40\,\rm m}(0.05) \simeq 85$ s.

FAST Core Array UHF-band. For the UHF band, the FoV is still restricted by the 40 m dish. We adopt the FoV of the 40 m dish at the redshift of 0.35, i.e., with a diameter of 24 arcmin, as the FoV for UHF-band interferometer DS survey. With a 4 hr DS observation, the interferometer observation covers a sky stripe with an area of $\delta S \simeq 24$ arcmin $\times$ 60 deg $\simeq 24$ deg^2 and the integration time per beam area is $\delta t \simeq t_{\rm bm}^{40\,\rm m}(0.35) \simeq 109$ s.

3.2. On-the-fly Survey

OTF observation is an efficient imaging technique that is widely used for deep-field surveys. By continuously collecting data as the telescope moves, OTF avoids the time-consuming stops and repositioning required in traditional point-by-point observations, significantly improving observational efficiency. In the OTF mode, the telescope scans the target region along R.A. or decl. at a constant speed (e.g., 15 arcsec s^{-1} along decl. direction, Jiang et al. 2020), while the receiver records signals with high temporal resolution. Each sampling point is accurately tagged with its celestial coordinates based on the telescope's real-time position. Compared to the DS observing mode, the OTF observing mode is not limited by the sky's rotation speed, allowing for more flexible scanning of localized sky regions. This makes it particularly suitable for deep-field surveys of specific areas. Systematic changes that occurred from OTF observation are more benign and easier to correct than drifts across a single map field (Mangum et al. 2007).

The comprehensive temporal budget for an OTF observation extends beyond mere "on-source" integration, encompassing

requisite "off-source" integrations and operational overhead, which includes the positional transits to and from the "OFF" reference, along with approach and transition phases (Sawada et al. 2008). In an idealized scenario where overhead is negligible, the optimal "off-source" integration timescales proportionally to the "on-source" integration time, with a scaling factor of $\sqrt{N_{\rm on-off}}$, where $N_{\rm on\text{-}off}$ represents the ratio of "on-source" to "off-source" measurements (Sawada et al. 2008; Mangum et al. 2007). For this analysis, we posit a scenario wherein the total integration time is sufficiently ample, exemplified by an initial allocation of 100 hr, and that this entire time is effectively utilized for target area observation.

Therefore, for a target observational region $S_{\rm area}$ and total survey time $t_{\rm tot}$, the integration time of the pixel by OTF mode can simply be estimated as:

$$\Delta t = \frac{t_{\rm tot}}{S_{\rm area}/{\rm FoV}}. \quad (10)$$

4. Results and Discussion

4.1. Drift Scan Observation Mode

Due to the contamination of Global Navigation Satellite Systems (GNSS; Teunissen & Montenbruck 2017), the frequency ranges of 1135–1310 MHz are mostly flagged. Therefore, the effective frequency range according to RFI flagging for current *L*-band equipment is 1050-1135 MHz (low-frequency band) and 1310–1450 MHz (high-frequency band) (Li et al. 2023), corresponding to the redshift range 0.25–0.35 and 0–0.08, respectively. This segmentation introduces non-uniform cosmic volume coverage, with the low-frequency sub-band probing higher redshifts (more distant galaxies) and the high-frequency sub-band targeting lower redshifts.

To effectively demonstrate the capabilities of FAST and the FAST Core Array, we predicted the observable H I galaxy number density across varying total survey areas and integration times. We considered three survey area scenarios based on different zenith angles from the FAST site: Near, Optimal, and Maximum.

1. Near Zenith Survey: When the telescope focuses on a small area within 2° of the FAST site's zenith, the survey area is approximately 200 $\deg^2$.
2. Optimal Survey: According to Jiang et al. (2020), the system temperature of FAST reaches its minimum at the maximum zenith angle of 15°, resulting in a survey area of approximately 1600 $\deg^2$.
3. Maximum Survey: Limited by the maximum zenith angle of FAST at 40° (Li et al. 2018), the maximum survey area is approximately 4000 $\deg^2$.

Three total stripe counts ($N_{\rm tot} = 90$, $N_{\rm tot} = 360$, $N_{\rm tot} = 720$), approximating observation periods of three months, one year, and two years, were also considered.

The predicted H I galaxy number densities in one-year DS survey are shown in Figure 4(a). As shown in the figure, the H I galaxy number density detected by FAST exhibits a significant decline with increasing redshift, particularly in the *L*-band. Within the optimal survey area, the high-frequency sub-band achieves a number density of approximately $\sim 10^{-1}$ $(h^{-1}\,{\rm Mpc})^{-3}$, while the low-frequency sub-band yields a substantially lower density of around $\sim 10^{-4}$ $(h^{-1}\,{\rm Mpc})^{-3}$, representing a difference of approximately three orders of magnitude. However, the implementation of an upgraded PAF leads to a notable increase in the number density, reaching approximately $\sim 10^{-3}$ $(h^{-1}\,{\rm Mpc})^{-3}$ at $z = 0.35$. Additionally, the decline in number density with increasing redshift becomes more gradual compared to the *L*-band. Indicating that FAST detectability of distant galaxies can be improved with the UHF PAF. As we expected, the Maximum Survey obtains a lower figure than that of the Optimal Survey, which is further lower than the Near Zenith Survey. Since a smaller survey area implies a longer integration time per pixel, thereby extending the detectable galaxy distribution to higher redshifts.

For the FAST Core Array, a significant improvement is observed, particularly at higher redshifts. For instance, the number density in the optimal survey area increases to $\sim 10^{-1}$ $(h^{-1}\,{\rm Mpc})^{-3}$at $z = 0.35$ and continues to exceed $\sim 10^{-3}$ $(h^{-1}\,{\rm Mpc})^{-3}$ up to $z = 1$. In comparison, LOWZ and CMASS sample together gives a density of order 3×10^{-4} $(h^{-1}\,{\rm Mpc})^{-3}$ at $z \sim 0.6$ (Ahn et al. 2012)

The predicted H I galaxy number densities carried out in the Optimal Survey area are shown in Figure 4(b). As depicted in the figure, longer observation time improves the SNR of galaxy sources, resulting in significantly larger number density. For instance, the number density of two-year observation is about an order of magnitude larger than that of three-month in both the low-frequency and high-frequency sub-bands. FAST Core Array demonstrates substantially higher number densities than FAST, about three orders in the *L*-band and two orders in the UHF-band. This persistent performance across both low- and high-redshift regimes highlights the Core Array's superior suitability for galaxy surveys compared to the single-dish architecture.

4.2. On-the-fly Observation Mode

The OTF observation mode provides a flexible scanning strategy, allowing surveys across various sky areas, up to FAST's maximum observable region of 16,700 $\deg^2$ after masking the Galactic plane. Figure 5(a) presents the H I galaxy number density distributions for both FAST and the Core Array in the L-band, covering two redshift ranges: low-z ($z = 0.01$–0.08) and high-z ($z = 0.25$–0.35).

At low redshift ($z = 0.01$–0.08), both FAST and the Core Array achieve sufficiently high H I galaxy number densities, peaking around $10^{-1}(h^{-1}{\rm Mpc})^{-3}$ for FAST when $t_{\rm tot} = 10^3$ hr and $S_{\rm area} = 10^3$ $\deg^2$. However, the number density saturates as

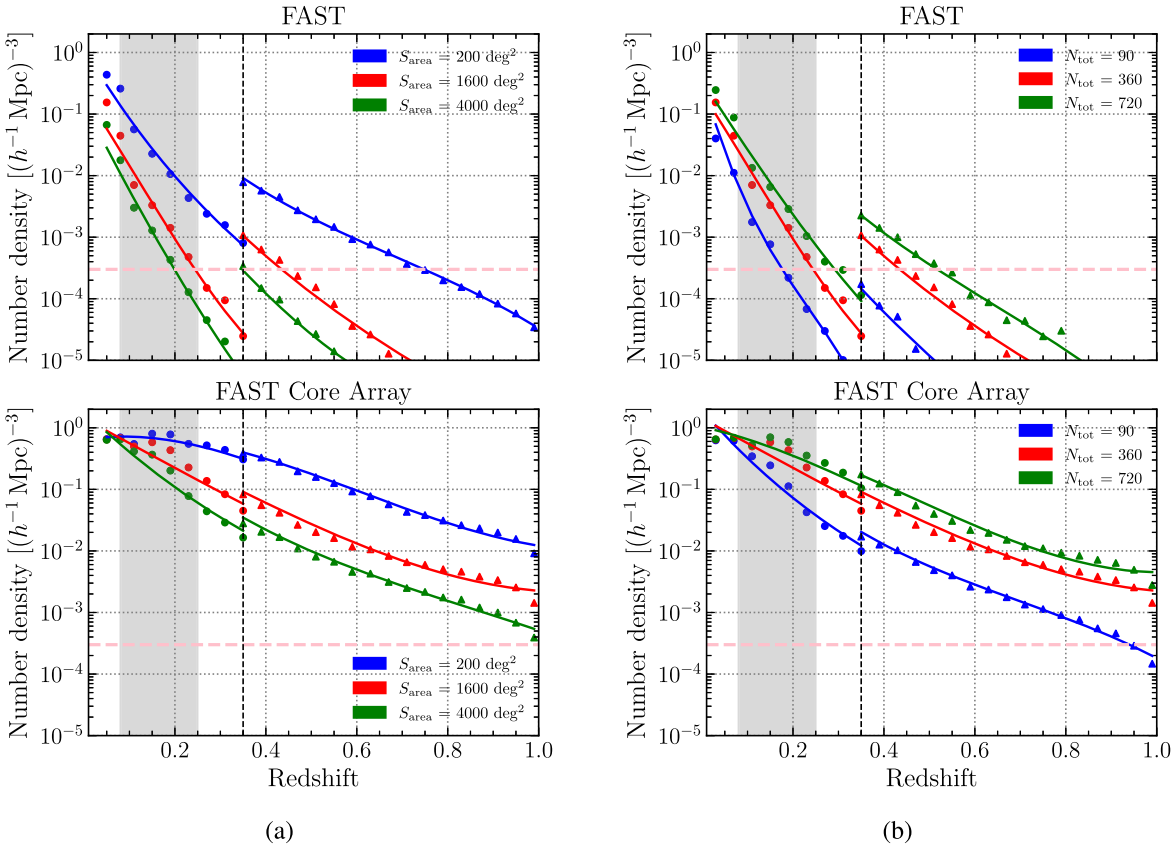

Figure 4. Galaxy number density in the DS survey for different survey areas and survey times. (a) Different survey areas, assuming $N_{\rm tot} = 360$, with $S_{\rm area} = 200$, 1600, and 4000 deg^2 shown in blue, red, and green; (b) different survey times, assuming $S_{\rm area} = 1600$ deg^2, with total observation times $N_{\rm tot} = 90$, 360, and 720 shown in blue, red, and green. The top and bottom panels show results for the FAST single-dish and Core Array, respectively. Solid lines in different colors represent the corresponding best-fit curves, modeled using the expression in Equation (13). The black dashed vertical line marks $z = 0.35$, separating the *L*-band (left) and UHF-band (right). The pink dashed horizontal line indicates a number density of 3×10^{-4} $(h^{-1}\mathrm{Mpc})^{-3}$, while the gray region represents the L-band frequency gap due to GNSS RFI.

integration time increases, with FAST reaching saturation at $t_{\rm tot} = 10^4$ hr when surveying its full sky coverage. The Core Array, due to its higher sensitivity, achieves saturation with a much shorter integration time of $t_{\rm tot} = 10^2$ hr. Despite the high number density, the limited cosmic volume at this redshift range makes it less useful for cosmological studies.

At high redshift ($z = 0.25$–0.35), the H I galaxy number density decreases significantly. For FAST, under $t_{\rm tot} = 10^3$ hr and $S_{\rm area} = 10^3$ deg^2, the density drops to $\sim 3 \times 10^{-4} (h^{-1}\mathrm{Mpc})^{-3}$, comparable to the LOWZ+CMASS sample, which serves as a reference for cosmological studies. The Core Array, however, maintains a much higher density of $\sim 10^{-1} (h^{-1}\mathrm{Mpc})^{-3}$ under the same conditions, making it a more effective choice for high-z H I surveys. This advantage stems from its superior sensitivity and larger effective aperture, which enhance the detection of faint H I signals even with shorter integration times.

Figure 5(b) extends the comparison to the UHF band, exploring H I galaxy number density distributions for FAST and the Core Array at higher redshifts ($z = 0.35$–0.65 and $z = 0.65$–1.00) under the OTF observing mode. As expected, both systems exhibit lower number densities compared to their *L*-band performance due to the decreasing H I signal strength at higher redshifts.

At intermediate redshifts ($z = 0.35$–0.65), the Core Array achieves a number density of $\sim 10^{-1} (h^{-1}\mathrm{Mpc})^{-3}$ with $t_{\rm tot} = 10^3$ hr and $S_{\rm area} = 10^2$ deg^2. Even when scaling up to FAST's maximum accessible survey area (black dashed line in Figure 5(b)), the Core Array maintains a density above the LOWZ +CMASS sample's reference value of $\sim 3 \times 10^{-4} (h^{-1}\mathrm{Mpc})^{-3}$. In contrast, under the same observing conditions, FAST's number density falls below this threshold at $S_{\rm area} = 10^3$ deg^2, limiting its effectiveness for cosmological applications.

At higher redshifts ($z > 0.65$), the contrast between the two systems becomes even more pronounced. The Core Array continues to achieve detectable number densities ($> 3 \times 10^{-4} (h^{-1}\mathrm{Mpc})^{-3}$) with $t_{\rm tot} = 10^3$ h and $S_{\rm area} = 10^3$ deg^2, whereas

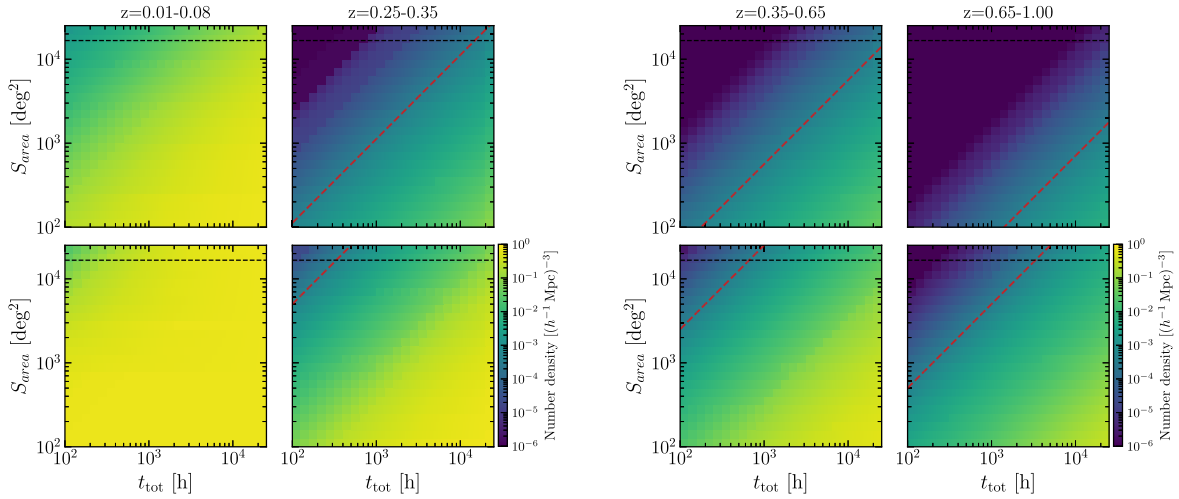

Figure 5. Galaxy number density in the OTF survey as a function of total survey area and integration time. (a) *L*-band results for redshift ranges $z = 0.01$–0.08 (left) and $z = 0.25$–0.35 (right). (b) UHF-band results for $z = 0.25$–0.35 (left) and $z = 0.65$–1.00 (right). The top panels show FAST single-dish results, while the bottom panels show those of the FAST Core Array. The black dashed line marks FAST's maximum observable survey area (∼16,700 deg^2) after Galactic plane masking. The red dashed line indicates a number density of 3×10^{-4} $(h^{-1}$ Mpc$)^{-3}$.

FAST's number density drops to $\sim 10^{-5}(h^{-1}\mathrm{Mpc})^{-3}$, falling below the critical threshold for reliable BAO detection. This stark disparity highlights the Core Array's superior capability for high-redshift H I surveys, driven by its advanced multi-beam interference suppression and aperture synthesis techniques, which enhance sensitivity to diffuse H I emission.

4.3. H I Power Spectrum Error

The power spectrum is a widely used statistical tool in LSS studies. In this subsection, we present an error forecast for the H I galaxy survey's power spectrum measurement. The primary sources of uncertainty arise from cosmic variance and shot noise. The fractional error in the power spectrum, evaluated over a wavenumber bin of width Δk, is given by (Feldman et al. 1994; Duffy et al. 2008),

$$\frac{\sigma_P}{P} = \sqrt{2\frac{(2\pi)^3}{V_{\mathrm{eff}}}\frac{1}{4\pi k^2 \Delta k}}\,\frac{P(k) + 1/n}{P(k)}, \tag{11}$$

where the effective survey volume is defined as

$$V_{\mathrm{eff}}(k) = \int \left[\frac{n(r)P(k)}{n(r)P(k)+1}\right]^2 d^3r, \tag{12}$$

with $n(r)$ representing the detected galaxy number density. Here, $P(k)$ denotes the matter power spectrum at wavenumber k, which we compute using CAMB.[6] In this analysis, we use $\Delta k/k = 0.125$.

[6] https://camb.info

To model the redshift dependence of the number density, we adopt a polynomial fitting approach:

$$\log_{10}(n(z)) = az^3 + bz^2 + cz + d. \tag{13}$$

The function $n(z)$ was fitted to the galaxy number density for each survey strategy. The best-fit $n(z)$ for DS surveys is shown as solid curves in Figures 4(a) and (b). We then convert redshift into comoving distance and incorporate this relation into the power spectrum analysis. This approach ensures a more accurate estimation of power spectrum uncertainties across different redshift bins.

4.3.1. Drift Scan Observation

The fractional errors of the power spectrum for the DS survey are shown in Figure 6(a) (*L*-band) and Figure 6(b) (UHF-band). We fix the total observation time at $N_{\mathrm{tot}} = 360$ and present results for survey areas $S_{\mathrm{area}} = 200$, 1600, and 4000 deg^2, shown in blue, orange, and green, respectively. The top and bottom panels in each figure correspond to results from the FAST single-dish survey and the FAST Core Array, respectively.

At low redshift ($0.01 < z < 0.08$), both the FAST single-dish and Core Array surveys achieve high galaxy number densities, making cosmic variance the dominant source of uncertainty in the power spectrum measurement. However, due to the limited cosmic volume at these redshifts, the power spectrum measurement is primarily restricted to small scales, with sensitivity concentrated at $k \gtrapprox 0.1\,h\,\mathrm{Mpc}^{-1}$.

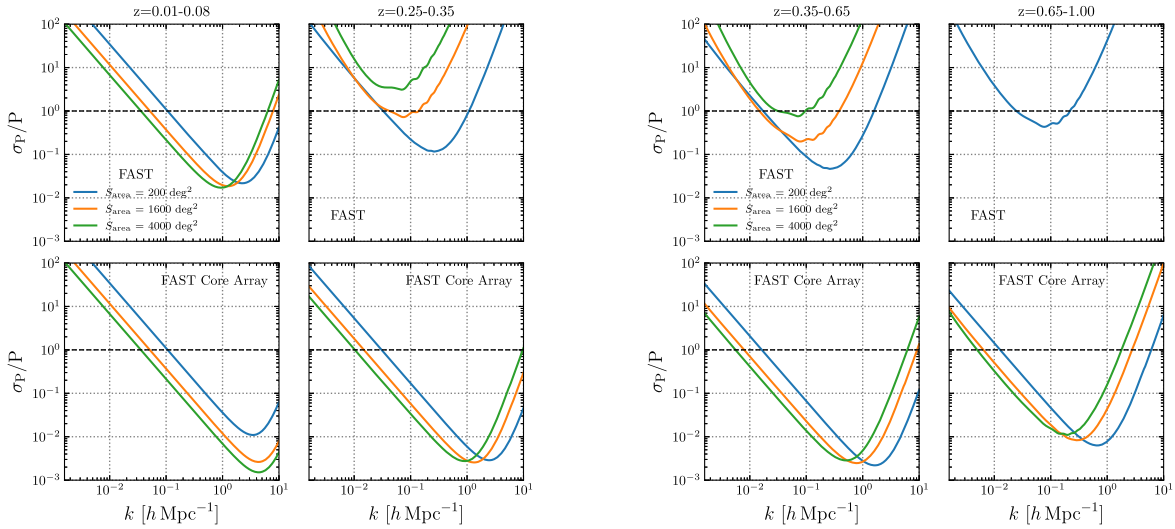

(a) (b)

Figure 6. Fractional error in the power spectrum for the DS observation with $N_{\rm tot} = 360$ for survey areas $S_{\rm area} = 200$, 1600, and 4000 deg^2. (a) L-band results with the left and right panels correspond to redshift ranges $z = 0.01$–0.08 and $z = 0.25$–0.35, separated by GNSS RFI contamination. (b) UHF-band results. The left and right panels correspond to redshift ranges $z = 0.35$–0.65 and $z = 0.65$–1.00. The top and bottom panels show results for the FAST single-dish and Core Array, respectively. The black dashed horizontal line marks $\sigma_P/P = 1$.

As redshift increases, the fractional errors in the power spectrum for the FAST single-dish survey grow significantly, particularly in the higher-redshift range of the L-band ($0.25 < z < 0.35$) and across the UHF-band ($0.35 < z < 1.00$). This increase is primarily due to a sharp decline in the number density of detected H I galaxies, which reduces the statistical power of the measurement. For $S_{\rm area} = 200\,{\rm deg}^2$, the errors exceed unity ($\sigma_P/P > 1$) at large scales in the UHF band, making power spectrum constraints challenging.

In contrast, the FAST Core Array provides significantly improved power spectrum measurements at higher redshifts. With its higher sensitivity and angular resolution, the Core Array achieves a sufficient H I galaxy number density even at large distances. At high redshifts ($z > 0.25$), the increased survey volume further reduces cosmic variance, enabling robust power spectrum detection across a wider range of scales. Notably, the Core Array is capable of probing large scales ($k \sim 0.1\,h\,{\rm Mpc}^{-1}$) while maintaining sensitivity at small scales ($k > 1\,h\,{\rm Mpc}^{-1}$).

In addition, we investigate the fractional errors in the H I power spectrum for different DS survey observation times. The results are presented in Figure 7(a) for the L-band and Figure 7(b) for the UHF-band, both assuming a fixed survey area of $S_{\rm area} = 1600\,{\rm deg}^2$.

The top panels of Figures 7(a) and (b) show the results for the FAST single-dish observation. As the total observation time increases up to $N_{\rm tot} = 720$, equivalent to two years of continuous observation, the single-dish survey achieves limited power spectrum detection up to redshift $z \sim 0.65$. However, the measurements remain largely dominated by cosmic variance and shot noise, significantly limiting their statistical precision, particularly at high redshift. At $z > 0.35$, the signal-to-noise ratio deteriorates, making it challenging to extract reliable cosmological information from the observed H I fluctuations.

In contrast, the bottom panels of Figures 7(a) and (b) illustrate the results for the FAST Core Array. Due to its superior sensitivity and angular resolution, the Core Array enables robust power spectrum measurements extending up to $z \sim 1$. Even at higher redshifts, where the H I signal is weaker and the number density decreases, the Core Array maintains a significantly lower fractional error compared to the single-dish mode. This enhanced capability makes it a powerful tool for probing large-scale structure evolution and constraining cosmological parameters across a wide redshift range.

4.3.2. *On-the-fly Observation*

We further investigate the fractional errors of the H I power spectrum using OTF observations, considering different survey areas and observation times.

We first fix the total observation time at $t_{\rm tot} = 1000\,{\rm hr}$ and vary the survey area among $S_{\rm area} = 200$, 1600, and 4000 deg^2. The corresponding results for the L-band and UHF-band are presented in Figures 8(a) and (b), respectively.

Similar to the DS observations, in the redshift range $0.01 \leqslant z \leqslant 0.08$, both the FAST single-dish and Core Array configurations yield significant detections of the H I power

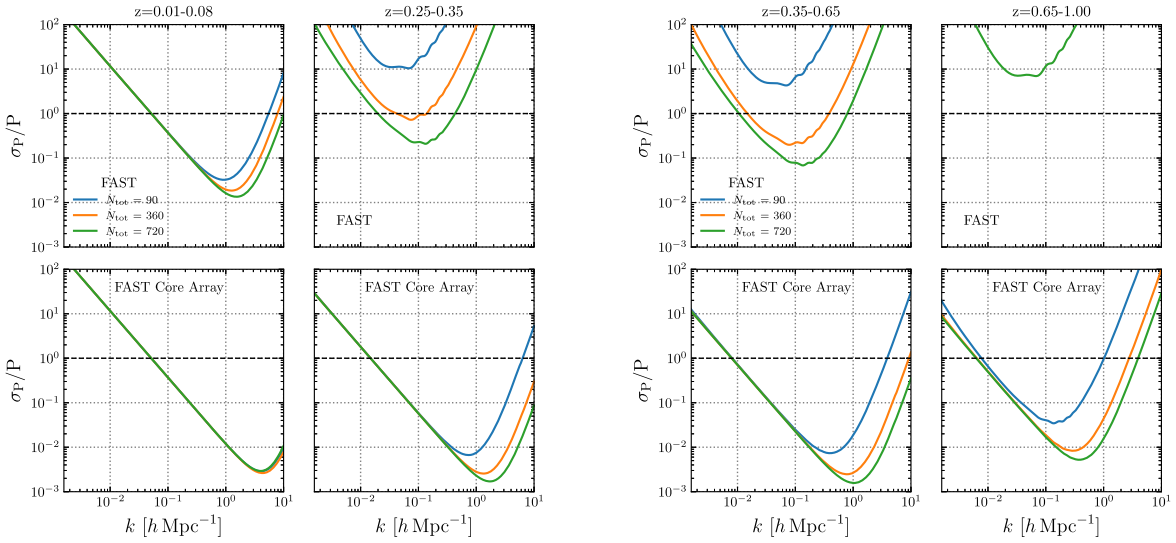

Figure 7. Projected fractional error in the power spectrum for the DS survey with $S_{\rm area} = 1600$ deg^2 for total observation times $N_{\rm tot} = 90$, 360, and 720. (a) L-band results with the left and right panels correspond to redshift ranges $z = 0.01$–0.08 and $z = 0.25$–0.35, separated by GNSS RFI contamination. (b) UHF-band results. The left and right panels correspond to redshift ranges $z = 0.35$–0.65 and $z = 0.65$–1.00. The top and bottom panels show results for the FAST single-dish and Core Array, respectively. The black dashed horizontal line marks $\sigma_P/P = 1$.

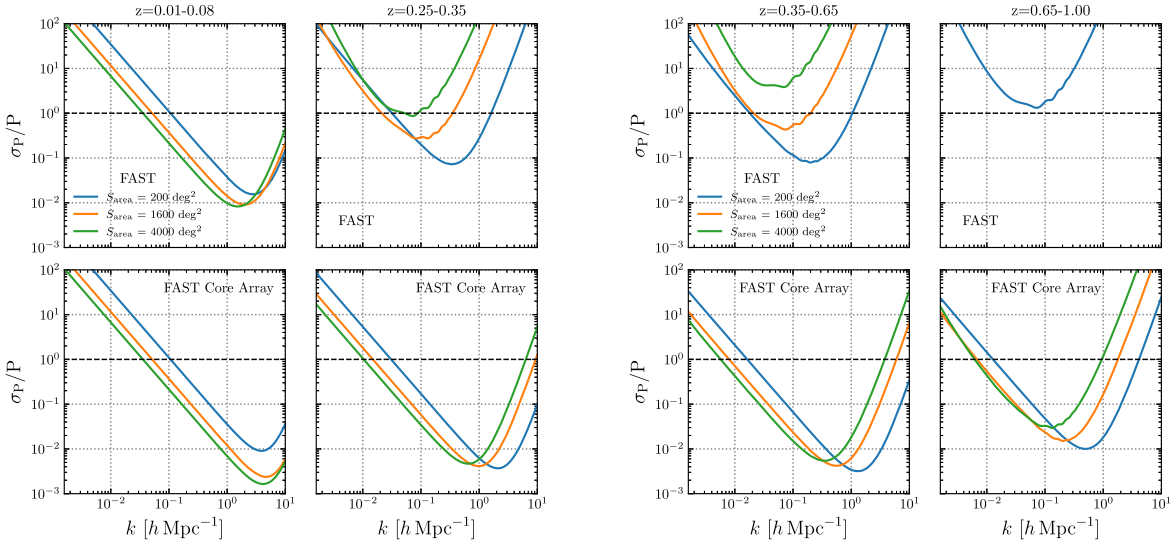

Figure 8. Fractional error in the power spectrum for the OTF survey with $t_{\rm tot} = 1000$ hr for survey areas of $S_{\rm area} = 200$, 1600, and 4000 deg^2. (a) L-band results with the left and right panels correspond to redshift ranges $z = 0.01$–0.08 and $z = 0.25$–0.35, separated by GNSS RFI contamination. (b) UHF-band results. The left and right panels correspond to redshift ranges $z = 0.35$–0.65 and $z = 0.65$–1.00. The top and bottom panels show results for the FAST single-dish and Core Array, respectively. The black dashed horizontal line marks $\sigma_P/P = 1$.

spectrum. Due to the limited cosmic volume at these low redshifts, most detections occur at small scales ($k \gtrsim 0.1\,h\,{\rm Mpc}^{-1}$), where the sample variance is minimized.

At higher redshifts, the fractional errors in the H I power spectrum increase substantially for the FAST single-dish observation. The decrease in detected H I galaxy number

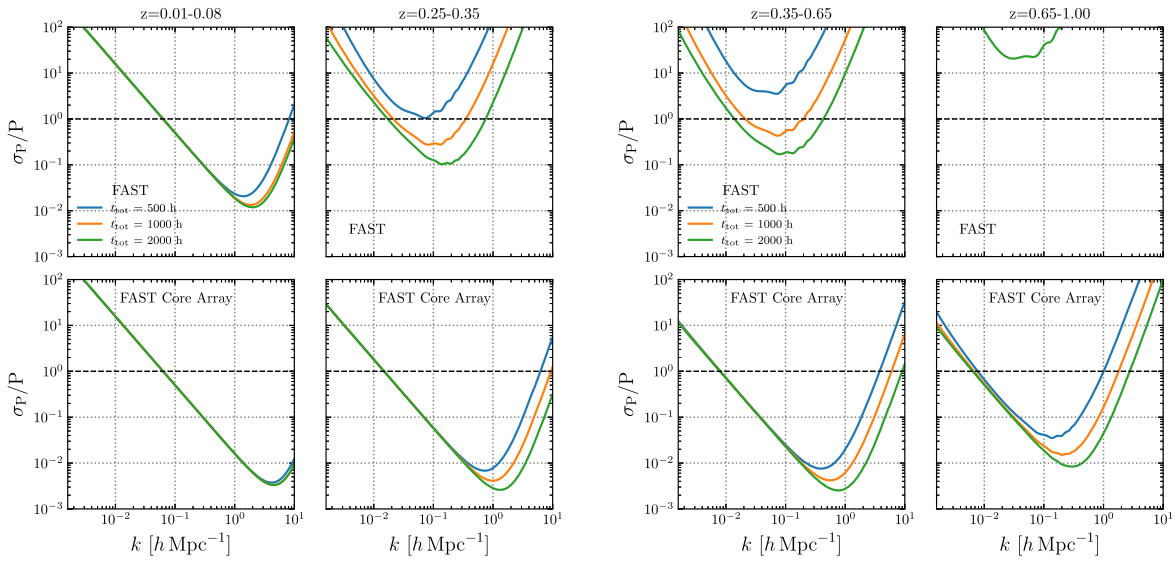

Figure 9. Fractional error in the power spectrum for the OTF survey with $S_{\rm area} = 1600\,{\rm deg}^2$ for total observation times of $t_{\rm tot} = 500$, 1000, and 2000 hr. (a) L-band results with the left and right panels correspond to redshift ranges $z = 0.01$–0.08 and $z = 0.25$–0.35, separated by GNSS RFI contamination. (b) UHF-band results. The left and right panels correspond to redshift ranges $z = 0.35$–0.65 and $z = 0.65$–1.00. The top and bottom panels show results for the FAST single-dish and Core Array, respectively. The black dashed horizontal line marks $\sigma_P/P = 1$.

density results in shot-noise-dominated uncertainties, making power spectrum measurements highly sensitive to galaxy shot noise rather than cosmological signals. Consequently, expanding the survey area does not significantly improve the measurement precision for the FAST single-dish mode.

In contrast, the FAST Core Array achieves a notable improvement in power spectrum measurements, particularly at higher redshifts. Its enhanced sensitivity and spatial resolution allow for more reliable detections of the H I power spectrum, highlighting its advantage in probing large-scale structure evolution beyond $z > 0.35$.

Next, we examine the effect of varying the total observation time on power spectrum measurements. We fix the survey area at $S_{\rm area} = 1600\,{\rm deg}^2$ and consider total observation times of $t_{\rm tot} = 500$, 1000, and 2000 h. The results for the L-band and UHF-band are displayed in Figures 9(a) and (b), respectively.

At low redshifts ($0.01 \leqslant z \leqslant 0.08$), increasing the integration time provides little improvement in power spectrum measurements. This is because the H I galaxy number density saturates at these redshifts, and the dominant source of uncertainty is cosmic variance rather than shot noise.

At higher redshifts ($z > 0.35$), increasing the observation time leads to a noticeable reduction in fractional errors, especially for the FAST single-dish mode. However, despite this improvement, the single-dish configuration still struggles to provide sufficiently precise power spectrum measurements for strong cosmological constraints. For the FAST Core Array, increasing the integration time significantly enhances detection precision.

Our analysis demonstrates that survey strategies play a crucial role in optimizing H I power spectrum measurements. At low redshifts, both the FAST single-dish and Core Array configurations perform well, with small-scale detections benefiting from high galaxy number density. However, at higher redshifts, the FAST Core Array significantly outperforms the single-dish mode, particularly when increasing the survey area and observation time. While longer integration times enhance sensitivity, their impact diminishes beyond a certain threshold, emphasizing the need for an optimal balance between survey area, integration time, and detection strategy in future H I galaxy surveys.

5. Summary and Conclusion

In this work, we have explored various strategies for conducting H I galaxy redshift surveys with the FAST telescope and its proposed Core Array configuration. Through semi-analytical simulations, we assessed the impact of different observational modes, survey areas, and integration times on the detectability of H I galaxies and the accuracy of power spectrum measurements.

We assume that surveys using the L-band and UHF-band are conducted separately. Since the beam size varies across each frequency band, we adopt the beam size at the highest frequency of each band for analysis, corresponding to a

redshift of 0.05 for the L-band and 0.35 for the UHF-band. As redshift increases, the beam size grows, leading to a larger scan strip coverage and increased integration time per beam. To simplify computations, we assume a constant beam size across each frequency band in the subsequent analysis, providing a conservative prediction.

Comparing the FAST single-dish mode with the FAST Core Array, we find that the single-dish mode achieves significant H I detections at low redshifts ($z \lesssim 0.35$), but its performance deteriorates at higher redshifts due to its lower sensitivity and larger beam size, which result in increased shot noise contamination. In contrast, the FAST Core Array, with its improved sensitivity and angular resolution, maintains a higher H I galaxy number density, particularly at $z > 0.35$, making it better suited for cosmological studies. The Core Array remains effective for BAO measurements at high redshifts, while the single-dish mode falls below the critical detection threshold.

Regarding observational strategies, we compare the DS and OTF modes. The DS mode is constrained by Earth's rotation, which limits flexibility in sky coverage but enables efficient large-area surveys with minimal operational overhead. In contrast, the OTF mode provides greater flexibility, particularly for targeted deep-field surveys, allowing more uniform integration times and optimized sky coverage. Although OTF introduces additional observational overhead, its efficiency in deep-field mapping makes it a valuable approach for high-precision studies.

The performance of both FAST configurations varies significantly with redshift. At low redshifts ($z \sim 0.01$–0.08), both the single-dish and Core Array configurations achieve high H I number densities, making cosmic variance the dominant source of uncertainty in power spectrum measurements. Due to the limited cosmic volume at these redshifts, detections are primarily constrained to small scales ($k \gtrsim 0.1\,h\,\mathrm{Mpc}^{-1}$). At higher redshifts ($z > 0.35$), the FAST Core Array significantly outperforms the single-dish mode. The Core Array maintains detectable H I number densities and provides robust power spectrum constraints, whereas the single-dish observations become dominated by shot noise. Increasing the survey area does little to mitigate this limitation for the single-dish mode, whereas it improves the performance of the Core Array.

Our results highlight the importance of survey strategy in optimizing H I galaxy redshift surveys. The FAST single-dish mode is well-suited for low-redshift H I studies, particularly in wide-area surveys. However, for precision cosmology at higher redshifts, the FAST Core Array provides a substantial improvement, offering better sensitivity and enabling large-scale structure studies up to $z \sim 1$. The choice between DS and OTF modes depends on the specific scientific objectives. DS surveys are ideal for wide-area coverage, while OTF observations are better suited for targeted deep-field studies.

Future work should focus on refining survey designs based on real observational constraints, including potential instrumental systematics and calibration strategies. Additionally, integrating H I intensity mapping techniques with resolved H I galaxy detections could further enhance the scientific output of FAST and its Core Array, providing valuable constraints on the evolution of large-scale structure and dark energy.

Acknowledgments

We sincerely thank Yun Liu and Wenxiang Pei for their valuable discussions and support in providing simulation data. We acknowledge the support of the National SKA Program of China (Nos. 2022SKA0110200 and 2022SKA0110203), the National Natural Science Foundation of China (NSFC, Nos. 12473091 and 12473001,), and 111 Project (No. B16009). Y.L. acknowledges the support of the Fundamental Research Funds for the Central Universities (No. N2405008). We express our gratitude to ChatGPT for its assistance in refining the manuscript and enhancing the code to improve execution efficiency.

ORCID iDs

Zhenglong Li https://orcid.org/0009-0004-0677-3474
Diyang Liu https://orcid.org/0009-0000-6895-9136
Chengliang Xu https://orcid.org/0009-0008-6933-358X
Yichao Li https://orcid.org/0000-0003-1962-2013
Xin Zhang https://orcid.org/0000-0002-6029-1933

References

Ahn, C. P., Alexandroff, R., Allende Prieto, C., et al. 2012, ApJS, 203, 21
Amiri, M., Bandura, K., Chen, T., et al. 2023, ApJ, 947, 16
Anderson, C. J., Luciw, N. J., Li, Y. C., et al. 2018, MNRAS, 476, 3382
Angulo, R. E., Springel, V., White, S. D. M., et al. 2012, MNRAS, 426, 2046
Ansari, R., Campagne, J. E., Colom, P., et al. 2012, A&A, 540, A129
Bagla, J. S., Khandai, N., & Datta, K. K. 2010, MNRAS, 407, 567
Bandura, K., Addison, G. E., Amiri, M., et al. 2014, Proc. SPIE, 9145, 914522
Barnes, D. G., Staveley-Smith, L., de Blok, W. J. G., et al. 2001, MNRAS, 322, 486
Battye, R. A., Browne, I. W. A., Dickinson, C., et al. 2013, MNRAS, 434, 1239
Battye, R. A., Davies, R. D., & Weller, J. 2004, MNRAS, 355, 1339
Bull, P., Ferreira, P. G., Patel, P., & Santos, M. G. 2015, ApJ, 803, 21
Carucci, I. P., Bernal, J. L., Cunnington, S., et al. 2024, arXiv:2412.06750
Chang, T.-C., Pen, U.-L., Bandura, K., & Peterson, J. B. 2010, Natur, 466, 463
Chang, T.-C., Pen, U.-L., Peterson, J. B., & McDonald, P. 2008, PhRvL, 100, 091303
Chen, X. 2012, IJMPS, 12, 256
Chen, Z., Chapman, E., Wolz, L., & Mazumder, A. 2023, MNRAS, 524, 3724
Cunnington, S., Li, Y., Santos, M. G., et al. 2023, MNRAS, 518, 6262
Duffy, A. R., Battye, R. A., Davies, R. D., Moss, A., & Wilkinson, P. N. 2008, MNRAS, 383, 150
Feldman, H. A., Kaiser, N., & Peacock, J. A. 1994, ApJ, 426, 23
Gao, L.-Y., Li, Y., Ni, S., & Zhang, X. 2023, MNRAS, 525, 5278
Giovanelli, R., Haynes, M. P., Kent, B. R., et al. 2005, AJ, 130, 2598
Giovanelli, R., Haynes, M. P., Kent, B. R., et al. 2007, AJ, 133, 2569
Han, Y., & Zhong, L. 2016, Int. J. Antennas Propagation, 2016, 5357368
Harper, S. E., Dickinson, C., Battye, R. A., et al. 2018, MNRAS, 478, 2416
Henriques, B. M. B., White, S. D. M., Thomas, P. A., et al. 2017, MNRAS, 469, 2626

Hu, W., Li, Y., Wang, Y., et al. 2021, MNRAS, 508, 2897
Hu, W., Wang, X., Wu, F., et al. 2020, MNRAS, 493, 5854
Irfan, M. O., Li, Y., Santos, M. G., et al. 2024, MNRAS, 527, 4717
Jiang, P., Chen, R., Gan, H., et al. 2024, AstTI, 1, 84
Jiang, P., Tang, N.-Y., Hou, L.-G., et al. 2020, RAA, 20, 064
Jin, S.-J., Wang, L.-F., Wu, P.-J., Zhang, J.-F., & Zhang, X. 2021, PhRvD, 104, 103507
Lang, R. H., Boyce, P. J., Kilborn, V. A., et al. 2003, MNRAS, 342, 738
Li, D., Wang, P., Qian, L., et al. 2018, IMMag, 19, 112
Li, J., Zuo, S., Wu, F., et al. 2020, SCPMA, 63, 129862
Li, Y., Santos, M. G., Grainge, K., Harper, S., & Wang, J. 2021, MNRAS, 501, 4344
Li, Y., Wang, Y., Deng, F., et al. 2023, ApJ, 954, 139
Li, Y.-C., & Ma, Y.-Z. 2017, PhRvD, 96, 063525
Liao, Y.-W., Chang, T.-C., Kuo, C.-Y., et al. 2016, ApJ, 833, 289
Lidz, A., Furlanetto, S. R., Oh, S. P., et al. 2011, ApJ, 741, 70
Liu, D., Li, Y., Tramonte, D., et al. 2024, arXiv:2411.03988
Loeb, A., & Wyithe, J. S. B. 2008, PhRvL, 100, 161301
Mangum, J. G., Emerson, D. T., & Greisen, E. W. 2007, A&A, 474, 679
Mao, Y., Tegmark, M., McQuinn, M., Zaldarriaga, M., & Zahn, O. 2008, PhRvD, 78, 023529
Masui, K. W., Switzer, E. R., Banavar, N., et al. 2013, ApJL, 763, L20
Matshawule, S. D., Spinelli, M., Santos, M. G., & Ngobese, S. 2021, MNRAS, 506, 5075
McQuinn, M., Zahn, O., Zaldarriaga, M., Hernquist, L., & Furlanetto, S. R. 2006, ApJ, 653, 815
MeerKLASS Collaboration, Barberi-Squarotti, M., Bernal, J. L., et al. 2025, MNRAS, 537, 3632
Meyer, M., Robotham, A., Obreschkow, D., et al. 2017, PASA, 34, 52
Meyer, M. J., Zwaan, M. A., Webster, R. L., et al. 2004, MNRAS, 350, 1195
Murphy, E. J., Bolatto, A., Chatterjee, S., et al. 2018, in ASP Conf. Ser. 517, Science with a Next Generation Very Large Array, ed. E. Murphy (San Francisco, CA: ASP), 3
Nan, R., & Li, D. 2013, MS&E, 1, 012022
Newburgh, L. B., Bandura, K., Bucher, M. A., et al. 2016, Proc. SPIE, 9906, 99065X
Ni, S., Li, Y., Gao, L.-Y., & Zhang, X. 2022, ApJ, 934, 83
Obreschkow, D., Croton, D., De Lucia, G., Khochfar, S., & Rawlings, S. 2009, ApJ, 698, 1467
Pan, J.-D., Wu, P.-J., Du, G.-H., Li, Y., & Zhang, X. 2025, JCAP, 2025, 080
Paul, S., Santos, M. G., Chen, Z., & Wolz, L. 2023, arXiv:2301.11943
Paul, S., Santos, M. G., Townsend, J., et al. 2021, MNRAS, 505, 2039
Pei, W., Guo, Q., Li, M., et al. 2024, MNRAS, 529, 4958
Perdereau, O., Ansari, R., Stebbins, A., et al. 2022, MNRAS, 517, 4637
Peterson, J. B., Aleksan, R., Ansari, R., et al. 2009, astro2010: The Astronomy and Astrophysics Decadal Survey, arXiv:0902.3091
Pritchard, J. R., & Loeb, A. 2008, PhRvD, 78, 103511
Pritchard, J. R., & Loeb, A. 2012, RPPh, 75, 086901
Saintonge, A. 2007, AJ, 133, 2087
Santos, M., Bull, P., Alonso, D., et al. 2015, in Proc. Advancing Astrophysics with the Square Kilometre Array (AASKA14) (Trieste: SISSA), 19
Santos, M. G., Cluver, M., Hilton, M., et al. 2017, arXiv:1709.06099
Sawada, T., Ikeda, N., Sunada, K., et al. 2008, PASJ, 60, 445
Seo, H.-J., Dodelson, S., Marriner, J., et al. 2010, ApJ, 721, 164
Spinelli, M., Carucci, I. P., Cunnington, S., et al. 2022, MNRAS, 509 2048
Springel, V. 2005, MNRAS, 364, 1105
Springel, V., Yoshida, N., & White, S. D. M. 2001, NewA, 6, 79
Square Kilometre Array Cosmology Science Working Group, Bacon, D. J., Battye, R. A., et al. 2020, PASA, 37, e007
Sun, S., Li, J., Wu, F., et al. 2022, RAA, 22, 065020
Switzer, E. R., Masui, K. W., Bandura, K., et al. 2013, MNRAS, 434, L46
Teunissen, P. J. G., & Montenbruck, O. 2017, Springer Handbook of Global Navigation Satellite Systems (Berlin: Springer)
Wang, J., Santos, M. G., Bull, P., et al. 2021, MNRAS, 505, 3698
Wolz, L., Abdalla, F. B., Alonso, D., et al. 2015, in Proc. Advancing Astrophysics with the Square Kilometre Array (AASKA14) (Trieste: SISSA), 35
Wolz, L., Blake, C., Abdalla, F. B., et al. 2017, MNRAS, 464, 4938
Wolz, L., Pourtsidou, A., Masui, K. W., et al. 2022, MNRAS, 510, 3495
Wu, F., Li, J., Zuo, S., et al. 2021, MNRAS, 506, 3455
Wu, P.-J., Li, Y., Zhang, J.-F., & Zhang, X. 2023a, SCPMA, 66, 270413
Wu, P.-J., Shao, Y., Jin, S.-J., & Zhang, X. 2023b, JCAP, 2023, 052
Wu, P.-J., & Zhang, X. 2022, JCAP, 2022, 060
Wyithe, J. S. B., & Loeb, A. 2008, MNRAS, 383, 606
Wyithe, J. S. B., Loeb, A., & Geil, P. M. 2008, MNRAS, 383, 1195
Xu, C., Deng, F., Xu, Y., & Chen, X. 2025, in press
Xu, Y., Wang, X., & Chen, X. 2015, ApJ, 798, 40
Xue, M., Zhu, W., Wu, X., Xu, R., & Wang, H. 2023, RAA, 23, 095005
Yang, W., Wolz, L., Li, Y., et al. 2024, arXiv:2412.08173
Zhang, C.-P., Zhu, M., Jiang, P., et al. 2024, SCPMA, 67, 219511
Zhang, J.-F., Gao, L.-Y., He, D.-Z., & Zhang, X. 2019, PhLB, 799, 135064
Zhang, M., Li, Y., Zhang, J.-F., & Zhang, X. 2023, MNRAS, 524, 2420
Zhang, M., Wang, B., Wu, P.-J., et al. 2021, ApJ, 918, 56
Zhao, X., Li, Y., Yang, W., et al. 2024, AJ, 169, 265
Zwaan, M. A., Meyer, M. J., Webster, R. L., et al. 2004, MNRAS, 350, 1210